

Imaging and Spatially Resolved Spectroscopy of AFGL 2688 in the Thermal Infrared Region ¹

Miwa Goto², Naoto Kobayashi, and Hiroshi Terada

Subaru Telescope, 650 North A'ohoku Place, Hilo, HI 96720

`mgoto@duke.ifa.hawaii.edu`

and

A. T. Tokunaga

Institute for Astronomy, University of Hawaii, Woodlawn Dr., Honolulu, HI 96822

ABSTRACT

We present ground-based high-resolution ($\sim 0''.3$) imaging of AFGL 2688 at L' ($3.8 \mu\text{m}$) and M' ($4.7 \mu\text{m}$). A wealth of structure in the central region is revealed due to less extinction in the thermal infrared. A clear border in the southern lobe at L' corresponds to the edge of the heavily obscured region in visible, indicating there is a dense material surrounding the central region. The images also show a narrow dark lane oriented to 140° east of north with the normal at 50° . The normal position angle is inconsistent with the optical polar axis ($\text{PA} = 15^\circ$), but is aligned to the high-velocity CO components found in the radio wavelength observations. The central star remains invisible at L' and M' . Several clumpy regions in the north lobe dominate in L' and M' luminosity. In particular a pointlike source (peak A) at $0''.5$ northeast of the center of the nebula exhibits the highest surface brightness with a very red spectral energy distribution (SED). Based on the almost identical SED as adjacent regions, we suggest that the pointlike source is not self-luminous, as was proposed, but is a dense dusty blob reflecting thermal emission from the central star.

We also present spatially resolved slit spectroscopy of the bright dusty blobs. An emission feature at $3.4 \mu\text{m}$ as well as at $3.3 \mu\text{m}$ is detected everywhere within our field of view. There is no spatial variation in the infrared emission feature (IEF) throughout the observed area ($0''.2$ – $1''.5$, or 240–1800 AU from the central source). The constant flux ratio of the emission feature relative to the continuum is consistent with the view that the blobs are mostly reflecting the light from the central star in the $3 \mu\text{m}$ region.

Subject headings: circumstellar matter — structure, dust — ISM: individual AFGL 2688) — ISM: dust : profiles — stars: AGB and post-AGB

1. Introduction

Low- to intermediate-mass stars ($2\text{--}5 M_{\odot}$) experience rapid transition from the asymptotic giant branch (AGB) to planetary nebula (PN) at the end of their life. An evolved star has high-mass loss when ascending the AGB, but at the tip of the AGB the star loses almost all the hydrogen envelope and cannot sustain high-mass loss. It then begins to evolve toward higher temperatures in H-R diagram while keeping almost constant luminosity as a proto-planetary nebula (PPN). The central star of the PPN eventually becomes hot enough ($>30,000$ K) to ionize the surrounding material ejected during the preceding mass-loss phase, and the PN is reached. The transition phase from PPN to PN is as short as about 5000 yr (Schönberner 1983). PPN share several observational properties in common (Kwok 1993, 2000), including a significant infrared excess at far-infrared wavelengths due to the warm circumstellar dust ($T_{\text{dust}} = 150\text{--}250$ K), a low-velocity molecular outflow ($10\text{--}20$ km s $^{-1}$), a central star that is typically an F- to G- type supergiant, and extended or bipolar nebulosity in the visible.

AFGL 2688 is a prototypical carbon-rich PPN, one of the most extensively studied so far since the discovery of reflection nebulosity (Ney et al. 1975). AFGL 2688 is located 1.0–1.5 kpc away from us (Cohen & Kuhi 1977) (hereafter we assume the distance to AFGL 2688 to be 1.2 kpc). From the visible spectroscopy at the reflection nebulosity, Crampton, Cowley, & Humphreys (1975) found that AFGL 2688 harbors an F5Ia star in the center of the nebula. It may have left the AGB only 200 years ago (Skinner et al. 1997).

In spite of many studies of AFGL 2688, the fundamental structure of the nebula is still actively debated. The old standard model requires equatorial density enhancement lying perpendicular to the polar axis to shape the optical bipolar nebula (Yusef-Zadeh, Morris, & White 1984; Latter et al. 1993; Lopez & Perrin 2000). The polar axis is defined by the optical bipolar nebula and lies at a position angle of about 15° . However, recent millimeter

¹Based on data collected at Subaru Telescope, which is operated by the National Astronomical Observatory of Japan.

²Visiting astronomer at the Institute for Astronomy, University of Hawaii

and centimeter radio observations have revealed features hard to reconcile with the standard model. These structures including a high velocity ^{13}CO flow (Yamamura et al. 1995), a compact expanding shell (Cox et al. 2000), and elongated emission (Jura et al. 2000), and all have a PA $\approx 55^\circ$. No present model can explain this apparent dual symmetry in AFGL 2688. Also surprising and unexplained is the quadrupole shape of the H_2 emission (Latter et al. 1993; Sahai et al. 1998a).

The goal of our observations is to better understand these apparently contradictory morphological features. We infer that the features at PA $\approx 55^\circ$ are young because they have relatively high velocity or are compact. To investigate the origin of these features, we must observe close to the central star. However, the inner $5''$ of the nebula suffers from heavy obscuration, and is virtually invisible at wavelengths shorter than $2\ \mu\text{m}$. Imaging in the thermal infrared region with a 8 m class telescope is essential to access the innermost region of AFGL 2688, as well as to provide high spatial resolution comparable with the visible image.

This paper is organized as follows: In §2 we describe the observations and reduction of the data. In §3 we summarize current understanding of AFGL 2688 and discuss several new and recently found morphological features.

2. Observations and Data Reduction

2.1. L' and M' Imaging

The imaging observations were made on UT 2001 July 14 at the Subaru Telescope with the Infrared Camera and Spectrograph (IRCS) (Tokunaga et al. 1998; Kobayashi et al. 2000). IRCS is a cryogenic camera and spectrograph equipped with two 1024×1024 InSb arrays. We used special L' - and M' -band filters optimized for the atmospheric transmission curve at Mauna Kea (Tokunaga, Simons, & Vacca 2001). Images of L' were recorded by $58\ \text{mas pixel}^{-1}$ camera ($60'' \times 60''$ field of view) at five different locations with the array offset by $30''$ to each time so that median sky frames could be made. The M' images were recorded in the same manner, but with the $22\ \text{mas pixel}^{-1}$ camera ($23'' \times 23''$ field of view) and smaller nodding offset ($10''$). The total on-source integration times were 270 and 360 s in L' - and M' , respectively. Flux calibration was facilitated by observing a photometric reference star, HD 201941, selected from Elias et al. (1982). The seeing was good (~ 0.3 in FWHM in L'), and stable throughout the observations. The actual spatial resolution at M' is somewhat inferior to the seeing FWHM because the high-resolution camera of IRCS was internally slightly out of focus.

The standard image reduction procedure was performed with IRAF.³ After sky subtraction, flat-fielding by dividing by a sky flat, and bad pixel correction, image frames were registered and averaged. We show the final images in Figures 1 and 2 in linear and logarithmic scales. Image convolution was applied with a 2D Gaussian filter of 1.4 pixels FWHM to show the faint nebulosity.

The L' and M' images look quite similar to each other. In addition to the spindle features commonly observed at the shorter wavelengths, they reveal great details in the innermost region for the first time. The upper part of south lobe close to the center is very faint in the 2.15 μm image taken by *HST/NICMOS* (Sahai et al. 1998a), but it is the brightest region in the southern lobe at the thermal infrared wavelength. The north lobe appears by far brighter near the center and harbors several bright blobs. A clear nebulosity enclosing the blobs extends farther to the east of the north lobe somewhat independently of the spindle shape. The peak surface brightness is measured at 6.2 mag arcsec⁻² and 4.4 mag arcsec⁻² at the southernmost bright blob at L' and M' , respectively. The total magnitudes are $L' = 5.5$ mag and $M' = 3.5$ mag. The central star is invisible in either wavelength, but a narrow dark lane lying 140° east of north in the center of the nebula was clearly detected in our image. The faint nebulosity extending about 6'' east of the north lobe roughly corresponds to the CO molecular outflow observed at 1.3 mm (Cox et al. 2000), suggesting shocked H₂ emission falls on the L' filter coverage.

We used *HST/NICMOS* archival data of AFGL 2688 obtained with H₂ continuum (2.15 μm) and *H*-band (1.65 μm) filters and our L' image to create a three-color composite image. The three images were registered at the brightest blob in the northern lobe. This could be inaccurate because the precise position of the surface brightness peak can be intrinsically different in each color, but we did not find any significant offset in the spindle pattern in the registered three images. The resultant composite image is shown in Figure 3 in different stretches.

2.2. 3 μm Spectroscopy

The spectroscopic observation was made on UT 2000 September 24 with the same instrument and telescope using the medium-resolution grism in the IRCS camera section. The slit was put along north to south at three different locations on the several bright blobs

³IRAF is distributed by the National Optical Astronomy Observatories, which are operated by the Association of Universities for Research in Astronomy, Inc., under cooperative agreement with the National Science Foundation.

in the northern lobe. The slit positions are illustrated in Figure 4. We used the $0''.3$ slit to match the excellent seeing of the night ($\sim 0''.25$ in FWHM) to obtain low-resolution ($R = 600\text{--}800$) spectra from 2.84 to $4.18\ \mu\text{m}$. The sky background was subtracted by nodding the telescope by $3''$ along the slit length. Special attention was paid to stay on one position for no longer than $60\ \text{s}$ to ensure good sky subtraction. The total on-source integration time was $140\ \text{s}$ at each slit position. We observed an F5V star (HR 1687, $V = 5.0$) as a spectroscopic standard at nearly the same airmass to cancel out the telluric absorption lines. The difference in the airmass between the object and the standard star was kept no larger than 0.1 so that the telluric transmission lines canceled well. Spectroscopic flat frames were obtained using a halogen lamp at the end of the night.

After we performed sky subtraction, flat-fielding, and correction of bad pixels in 2D spectrogram images, one-dimensional spectra were obtained using the aperture extraction package of IRAF. The width of the aperture was $0''.233$ (4 pixels), about the same size as the seeing. We defined the nine apertures within the slit offset by $0''.233$ from each other covering $\pm 1''$ from the center of the slit (Fig. 4).

Wavelength calibration was performed using over 60 telluric absorption lines. First, we calculated the model telluric transmission curve with matched spectral resolution using the ATRAN atmosphere modeling software (Lord 1992). Then the local minimums of the model curve were picked up to make a list of telluric lines. The result of fitting the observed atmospheric absorption lines with a calculated line list shows differences no more than $\pm 0.001\ \mu\text{m}$ in peak-to-peak all across the spectra. The intrinsic stellar lines of the spectral standard (mostly atomic hydrogen) were hard to remove because of the blending with the telluric absorption lines. Only $\text{Br}\alpha$ ($4.05\ \mu\text{m}$) and $\text{P}\text{f}\gamma$ ($3.74\ \mu\text{m}$) were fit with a Lorentzian profile and subtracted before dividing. The one-dimensional spectra were registered to the standard star spectrum by subpixel shifting. The small discrepancy in the airmass between the standard and the object was corrected by rescaling the spectra according to Beer’s law. Since the $0''.3$ slit width corresponds to 5 pixels, the spectra shown in Figure 5 were binned by 2 pixels. The spectrum of the standard star was assumed to be a Planck function of $T_{\text{eff}} = 6530\ \text{K}$, and the L' magnitude of the standard star was estimated using the color of an F5V star ($V - L = 1.35$) in Tokunaga (2000).

3. Discussion

3.1. Current Understanding of the Nebula’s Structure

A summary of our present understanding of AFGL 2688 is sketched in Figure 6. We focused our attention on recent observational studies of the morphology and kinematics of the nebula. A detailed discussion of models, such as the one by Skinner et al. (1997), are beyond the scope of this paper.

In the past decades, this nebula has been the one of the primary targets for new observing facilities and techniques. The central star has not been detected to date at any wavelength (but see Cox et al. 2000, who found a millimeter continuum peak). However, the location of the illumination source in the nebula is determined reasonably well by the center of the “searchlight beams” (Sahai et al. 1998b) and the symmetric center of the polarization map in the reflection nebula (Weintraub et al. 2000). In addition, the polarization center roughly coincides with the intersection of lines connecting blue- and redshifted components of multiple CO outflows (Cox et al. 2000). Low-velocity (10–20 km s⁻¹) winds associated with the mass loss have been detected in the study of molecular line kinematics at radio wavelengths (Young et al. 1992; Yamamura et al. 1995). The visible nebulosity is thought to be a remnant of mass loss when the star was still in the AGB phase.

In the context of the current standard model, the horns extending out of the lobes have been interpreted as limb brightening at the inner wall of the conical opening. However, Sahai et al. (1998b) found the edges of these searchlight beams are too sharp, and the contrast between searchlights and regions between the two searchlight beams are too high, to be reproducible by limb brightening. They argue that the sharp edge is not a product of a material distribution. They propose an obscuring “dust cocoon” with a nonuniform annular opening through which the central source is illuminating the entire nebula to produce the observed intensity distribution of the searchlight beams.

The concentric arcs around the nebula have been taken to be evidence of material ejected in the periodic mass loss caused by either unstable pulsation of the latest AGB phase or recent interaction with a close binary. With faint and detailed structures revealed by *HST/WFPC2*, Sahai et al. (1998b) found the arcs are almost partial circles with no additional elongation. They argue that the perfect circularity is not consistent with latitudinal density variations because the arcs should proceed faster in the lower-density medium to form more elongated curves along polar axis, which is not apparent in their images. The absence of latitudinal density variation in Sahai’s model is not consistent with the current standard model.

In the *H* and *K* the nebula lobes appears as two spindles capped with shocked H₂

emission blobs (Latter et al. 1993). The clear and bright spindle edge indicates bubbles invading the low-velocity wind sweeping up the circumstellar material. The axisymmetrical bubbles are probably infrared counterparts of the moderate-velocity wind ($\sim 40 \text{ km s}^{-1}$) detected in the radio wavelength (Young et al. 1992). They argued against radiation pressure acceleration to drive such a fast outflow by the dragging of dust grains.

The blue and red components of the radio outflow found in ^{13}CO observations are found along $\text{PA} = 60^\circ$ (Yamamura et al. 1995), rather than $\text{PA} = 15^\circ$ in the optical. Jura et al. (2000) have discovered the thermal emission tail of extremely large dust grains ($a \sim 0.5 \text{ cm}$) at centimeter wavelengths. The emitting region is elliptical in shape, with the major axis along $\text{PA} = 53^\circ$. An expanding shell-like structure of $2''$ diameter was found by Cox et al. (2000) in CO. The shell is slightly elongated to $\text{PA} = 54^\circ$. One of the puzzling features of the nebula is that the axis of symmetry of the optical and infrared lobes is at $\text{PA} = 15^\circ$, but the axis of symmetry at radio wavelengths is at $\text{PA} = 53^\circ\text{--}60^\circ$.

3.2. Sharp Edge in the Southern Lobe

What is recognized first in our three-color composite image (Fig. 3) is a clear border in the southern lobe with a striking color change in the infrared. The crosscut at the south edge along the optical bipolar axis is shown in Figure 7. The H and $2.15 \mu\text{m}$ flux drops sharply at $1''$ south from the center. The location of the border roughly corresponds to the edge of the dust cocoon proposed by Sahai et al. (1998a). The red color ($K - L' > 3$) suggests heavy reddening in the intervening dust cocoon. The sharpness of the limb implies an expanding cocoon into the circumstellar envelope pushing away the surrounding material. To allow bulletlike ejection of the bipolar bubbles, the cocoon would have to have formed after the lobes.

We noticed the spatial variation of the flux in Figure 7 in L' and M' is almost the same, and the similarity also holds for between H and $2.15 \mu\text{m}$, but it exhibits a huge difference between $2.15 \mu\text{m}$ and L' , indicating the specific grain size responsible for the reddening. To estimate the size of the grain and the amount of the extinction, we compare the flux density distribution observed at the cocoon and outside of the cocoon (Fig. 8). It is evident the visible light is totally obscured in the cocoon, while there is no significant color change attributable to the cocoon in the thermal infrared region, except that the flux density increases in the cocoon by order of 2. This indicates that the light from the central region is first scattered by the dust grains in the lobe, and then subject to extinction in the foreground dust cocoon surrounding the lobes. The flux density enhancement at thermal wavelengths could be attributed to the higher particle density closer to the center.

It is obvious that the extinction curve is quite different from the average interstellar medium. We calculated the extinction efficiency of amorphous carbon grains of various sizes using the optical constants for amorphous carbon retrieved from Zubko et al. (1996). We found the reddening property is best reproduced by $0.2 \mu\text{m}$ single-size spherical amorphous carbon grains, and it has a flat extinction in the visible wavelength, a large drop between 2 to $3 \mu\text{m}$ region, and an equally negligible extinction at L' and M' . We applied the reddening by the amorphous carbon to the flux density distribution observed outside the cocoon with column density of $N_{\text{dust}} = 1.5 \times 10^9 \text{ cm}^{-2}$. We found the resulting density distribution matches that inside the cocoon well (Fig. 9). The extinction applied in the cocoon corresponds to $A_V = 6.3 \text{ mag}$ in visible and $A_K = 2.7 \text{ mag}$ in K , where the optical depth was estimated from $\tau_\lambda = N_{\text{dust}} Q_{\text{ext}} \pi a^2$ and a is the particle radius.

3.3. Dark Lane at the Center of the Nebula

The smaller extinction at L' allows a view close of the central star through the heavily obscuring dust cocoon. At this wavelength a dark lane in the center of the nebula is evident (Fig. 10). This dark lane, which is seen at L' and M' , has a different orientation from the dust cocoon observed by Sahai et al. (1998b), and it appears to be perpendicular to the major axis of the centimeter continuum emission region observed by Jura et al. (2000).

The location of the central star proposed by the polarization map, searchlights, and the multiple outflow of CO molecules falls close to the dark lane, but there is no pointlike source at L' or M' corresponding to the central star. We infer the dark lane is a dust disk lying almost edge-on obscuring the central star. The similar appearance at L' and M' bands indicates it is absorbing light evenly at 3–5 μm . Dust grains in the disk should be cold enough compared to the surrounding nebulosity to produce no detectable emission at L' or M' . Hence the size of the grain should be quite large ($a > 1 \mu\text{m}$).

Although the nature of the disk is uncertain, there might be a physical association of the disk orientation to the morphological features observed in the radio wavelength oriented to $\text{PA} \approx 55^\circ$ (Fig. 6). The disk would collimate all these high-velocity compact components in a direction offset from the optical polar axis. The high velocity compact components should be the youngest structures in the nebula. We speculate that the central star is now experiencing a change in the symmetry axis. Consequently, the observed position angle of each component near the center may change depending on the time it formed. It is tempting to note the series of blobs in the northern lobe seems to curve from the northwest to the northeast from the center (Fig. 3). The sequence might be a tracer of explosive ejection from the central star in the order of formation. We might be witnessing the central star

gradually changing the ejection axis from $PA = 15^\circ$ to $PA \approx 55^\circ$.

3.4. The Nature of Peak A

An enigmatic object near the center of the nebula is peak A, a pointlike source at the northeast of the central star (Fig. 10). Based on the distorted polarization pattern near the peak, Weintraub et al. (2000) argued the peak A is a self-luminous infrared source that is a binary companion to the invisible central star. At first glance the extremely red color of peak A (Fig. 3) appears to be a clear signature of the thermal emission source, yet we find evidence to the contrary. We will discuss several observational features to suggest that the peak A is not self-luminous, but a dense dusty blob reflecting the infrared light from the central star.

First, although peak A is indeed the brightest spot, the overall look of the SED does not deviate from the surrounding reflection nebula. To see this, we compared the SED with those of adjacent regions (Fig. 11). The infrared (1.65–4.70 μm) SED of peak A and those extracted from other locations are almost identical. If peak A has an illuminating source inside seen through the enshrouding dust in the thermal infrared, it would be hard to account for the identical SED in the infrared as far as $2''.3$ (~ 2800 AU) away from peak A. The direct light should be much redder than the scattered one. The only plausible interpretation of the identical SEDs is the identical radiation mechanism, namely, the relevant region is illuminated by a single central infrared source, and the reflected light becomes redder in the foreground dust cocoon. There is obviously no sign of a pointlike source in the southern lobe where a similar SED is observed, and thus we conclude peak A is not a self-luminous point source either, but a dense dusty blob reflecting the illumination from the central infrared source.

Second, if peak A were indeed self-luminous, what kind of source could it be? Peak A is located ~ 600 AU away from the central star in the projected distance, so it cannot be thermal emission of dust heated up by the central star ($L_* = 1.8 \times 10^4 L_\odot$) in equilibrium (thermal equilibrium temperature is < 50 K). We may eliminate shock heating, because there is no shocked feature at the peak A in H_2 2.122 μm narrowband imaging by Sahai et al. (1998a). Hence the remaining possibility is an enshrouded star. The apparent earlier phase of evolution relative to the central star (no nebulosity association, no hydrogen emission lines) suggests the possible stellar source should be a G- to M-type main-sequence or AGB star. However, to date we have no observational support for the presence of such a late type star there. Spatially resolved spectroscopy in the near-infrared (1.1–2.4 μm) made by Hora & Latter. (1994) covers the peak A location, but there is no significant CO absorption

band-head at $2.3 \mu\text{m}$ in their spectra.

Third, our spectroscopy at peak A shows prominent emission features of hydrocarbon dust. Optically thick thermal emission cores are typically featureless, or at most exhibit molecular absorption lines in the $3.0 \mu\text{m}$ region due to C_2H_2 or HCN (Goto et al. 1997; Ridgway, Carbon, & Hall 1978) that are not apparent in our spectrum. As no AGB stars have been reported to have IEF in the $3 \mu\text{m}$ region, the hydrocarbon features are a consequence of scattered light originating from the central star.

Fourth, the observed hydrocarbon features are all uniform around peak A. The spectra presented in Figure 5 are normalized to the power-law continuum to see if there is any spatial variation in the hydrocarbon feature at 3.3 and $3.4 \mu\text{m}$, and this is shown in Figure 12. For comparison with the spectral feature extracted at each location along the slit, a template spectra is created by combining all the data available. We found all the normalized spectra are very similar, and there is no significant deviation from the template at any location within the observed area. This is again consistent with the view that the IEF emission source is remotely illuminating the dusty blobs, and we are observing the scattered light in the $3 \mu\text{m}$ region.

When scattered light is dominant at $3 \mu\text{m}$, it is surely so at the shorter wavelengths. However, the polarization map at $2.2 \mu\text{m}$ presented by Weintraub et al. (2000) shows lower polarization close to peak A. We suspect that multiple scattering in a dense dust blob can reproduce the same polarization pattern, namely, less polarization at the brighter location. Polarization imaging in the thermal infrared band, where the multiple scattering effects are smaller, would be more conclusive. We conclude that peak A is probably not a self-luminous source, but is instead one of the dust blobs reflecting infrared illumination from the central source.

4. Summary

We presented high-resolution ($\sim 0''.3$) L' and M' images of AFGL 2688. Imaging in the thermal infrared wavelength at high angular resolution proved to be a powerful technique to penetrate deep into the central region of a bipolar proto-planetary nebula with heavy extinction and that is invisible at shorter wavelengths. We conclude the following:

1. A dust cocoon described by Sahai et al. (1998b) appears as a very red region in the south lobe with a dramatic color change between 2 to $3 \mu\text{m}$. The amount of extinction in the dust cocoon was estimated to be $A_V = 6.3$ mag, assuming $0.2 \mu\text{m}$ amorphous carbon grains are responsible for the extinction.

2. We found a dark lane at the core of the nebula at $PA = 140^\circ$. The normal position angle is more consistent with a high-velocity outflows rather than an optical reflection nebula. The central star is invisible at both L' or M' .

3. Peak A, postulated to be a self-luminous object, has an almost identical SED to the nearby heavily obscured regions, and we conclude that it is not self-luminous.

4. From the $3\ \mu\text{m}$ spectra we find that the IEFs at the bright blobs look uniform, and exhibit no significant spatial variation in the feature-to-continuum ratio. This supports the idea that the bright blobs are reflecting light from the invisible central star.

We are grateful to M. Weber and R. Potter for their assistance when these observations were made. We appreciate many useful discussions with H. Suto. We thank the staff and crew of the Subaru Telescope for their valuable assistance in obtaining these data. M. Goto is supported by Japan Society for the Promotion of Science fellowship.

REFERENCES

- Cox, P., Lucas, R., Huggins, P. J., Forveille, T., Bachiller, R., Guilloteau, S., Maillard, J. P., & Omont, A. 2000, *A&A*, 353, L25
- Crampton, D., Cowley, A. P., & Humphreys, R. M. 1975, *ApJ*, 198, 135
- Cohen, M., & Kuhl L. 1977, *ApJ*, 213, 79
- Elias, J. H., Frogel, J. A., Matthews, K., & Neugebauer, G. 1982, *AJ*, 87, 1029
- Goto, M., Sasaki, Y., Imanishi, M., Nagata, T., & Jones, T. J. 1997, *PASJ*, 49, 485
- Hora, J. L., & Latter, W. B. 1994, *ApJ*, 437, 281
- Jones, T. J., & Dyck, H. M. 1978, *ApJ*, 220, 159
- Jura, M., Turner, J. L., Van Dyk, S., & Knapp, G. R. 2000, *ApJ*, 528, L105
- Kobayashi, N. et al. 2000, *Proc. SPIE*, 4008, 1056
- Kwok, S. 1993, *ARA&A*, 31, 63
- Kwok, S. 2000, *The Origin and Evolution of Planetary Nebulae*, Cambridge Astrophysics Series 31 (Cambridge: Cambridge University Press)

- Latter, W. B., Hora, J. L., Kelly, D. M., Deutsch, L. K., & Maloney, P.R. 1993, *AJ*, 106, 206
- Lopez, M., & Perrin, J.-M. 2000, *A&A*, 354, 657
- Lord, S. D. 1992 NASA Technical Memor. 103957
- Ney, E., Merrill, K. M., Becklin, E. E., Neugebauer, G., & Wynn-Williams, C. G. 1975, *ApJ*, 198, L129
- Ridgway, S. T., Carbon, D. F., & Hall, D. N. B. 1978, *ApJ*, 225, 138
- Sahai, R., Hines, D. C., Kastner, J. H., Weintraub, D. A., Trauger, J. T., Rieke, M. J., Thoupson, R. I., & Schneider, G. 1998a, *ApJ*, 429, 163
- Sahai, R. et al. 1998b, *ApJ*, 439, 301
- Schönberner, D. 1983, *ApJ*, 272, 708
- Skinner, C. J. et al. 1997, *A&A*, 327, 342
- Tokunaga, A. T. et al. 1998, *Proc. SPIE*, 3354, 512
- Tokunaga, A. T., Simons, D., & Vacca, W. D. 2001, *PASP*, in press.
- Tokunaga, A. T. 2000, in *Allen's Astrophysical Quantities*, ed. A. N. Cox, (4th ed., New York: Springer)
- Weintraub, D. A., Kastner, J. H., Hines, D. C., & Sahai, R. 2000, *ApJ*, 531, 401
- Young, K., Serabyn, G., Phillips, T. G., Knapp, G. R., Guesten, R., & Schulz, A. 1992, *ApJ*, 385, 265
- Yamanura, I., Onaka, T., Kamijo, F., Deguchi, S., & Ukita, N. 1995, *ApJ*, 439, 13
- Yusef-Zadeh, F., Morris, M., & White, R. L. 1984, *ApJ*, 278, 186
- Zubko, V. G., Mennella, V., Colangeli, L., & Bussoletti, E. 1996, *MNRAS*, 282, 132

Fig. 1.— Image of AFGL 2688 at L' ($3.8 \mu\text{m}$). North is up and East is the left. Left: shown in linear scale. The peak surface brightness and the total magnitude of the bipolar nebula are $6.2 \text{ mag arcsec}^{-2}$, and 5.5 mag , respectively. The spatial resolution is about $0''.3$. The image is convolved with a 2D Gaussian filter of 1.4 pixel FWHM to show the faint structure better. Right: the same, but shown in logarithmic scale.

Fig. 2.— The same as Fig. 1, but at M' ($4.7 \mu\text{m}$). The peak surface brightness and total magnitude are $4.4 \text{ mag arcsec}^{-2}$ and 3.5 mag , respectively. The seeing was about the same as at L' , but the actual spatial resolution is somewhat inferior because of the slightly out-of-focus $22 \text{ mas pixel}^{-1}$ camera at M' . The images are convolved with a 2D Gaussian filter of 1.4 pixel FWHM.

Fig. 3.— True-color composite image of AFGL 2688. Blue, green, and red represent H ($1.65 \mu\text{m}$) and H_2 continuum ($2.15 \mu\text{m}$) obtained with *HST/NICMOS*, and L' with the IRCS. Left: The image is normalized to the maximum intensity of the each band before combining into a color image. Right: The same, but with a different stretch to emphasize the color change $1''$ south from the tip of the southern lobe. The encircled regions are the locations of aperture photometry in Fig. 8.

Fig. 4.— L' contour plot of AFGL 2688 with an overlay showing the slit position for the grism spectroscopy.

Fig. 5.— Spatial variation in the $3 \mu\text{m}$ spectra of AFGL 2688 at the three locations illustrated in Fig. 4. The spectra are extracted at every $0''.233$ ($= 4 \text{ pixel}$) along the slit. The off-center spectra are offset by $2 \times 10^{-14} [\text{W m}^{-2} \mu\text{m}^{-1}]$ for clarity. The continua are defined by fitting both sides of the emission features ($2.95\text{--}3.15 \mu\text{m}$ and $3.60\text{--}3.80 \mu\text{m}$) with a power-law function.

Fig. 6.— A schematic view summarizing the major morphological features of AFGL 2688. The structural components described here can be divided into two distinct groups, one aligned to $\text{PA} = 15^\circ$ and the other to $53^\circ\text{--}60^\circ$. The concentric arcs, the searchlights, the delineated bipolar lobes, and the dust cocoon all detected at visible to near-infrared wavelengths (Sahai et al. 1998a,b; Latter et al. 1993) are aligned to $\text{PA} = 15^\circ$. The high-velocity (26.5 km s^{-1} at projected velocity) component of the ^{13}CO outflow (Yamamura et al. 1995), the compact expanding CO shell ($>10 \text{ km s}^{-1}$) (Cox et al. 2000), and the centimeter wavelength continuum emission (Jura et al. 2000) are aligned to $\text{PA} = 53^\circ\text{--}60^\circ$. The low-velocity wind ($10\text{--}20 \text{ km s}^{-1}$) is thought to be a remnant of spherical mass loss in the preceding AGB phase. The moderate-velocity wind ($\sim 40 \text{ km s}^{-1}$) might be associated to the near-infrared bipolar nebula invading the low-velocity wind (Young et al. 1992). Shocked H_2 molecule blobs are distributed orthogonally about the center to cap the optical bipolar lobes at the

tips. The CO multiple outflows apparently originating at the central source are aligned with the H₂ blobs but are not shown here (Cox et al. 2000).

Fig. 7.— Left: Crosscuts of the surface brightness of AFGL 2688 at the south edge at H (1.65 μm), and the H₂ continuum (2.15 μm), L' , and M' . The abscissa is an offset from the center along the optical bipolar axis (PA = 15°). The location of the edge where the surface brightness in the 2.15 μm sharply drops is marked with solid lines ($\sim 1''$ from the center). Right: A crosscut of the color variation ($H-2.15 \mu\text{m}$, $2.15 \mu\text{m}-L'$, and $L'-M'$) in magnitude unit at the same location as the left panel.

Fig. 8.— The aperture photometry inside and outside the dust cocoon. The aperture locations are marked in Fig. 3. The surface brightness outside the cocoon is reddened again by a 0.2 μm amorphous carbon grain to estimate the amount of extinction. The result is well matched to the surface brightness inside the cocoon after applying the extinction by $N_{\text{dust}} = 1.5 \times 10^9 \text{ cm}^{-2}$.

Fig. 9.— An extinction efficiency of an amorphous carbon grain. The extinction efficiency is calculated with Mie theory for a single-size ($a = 0.1 \mu\text{m}$ to $a = 2.0 \mu\text{m}$) spherical amorphous carbon grain at the specific wavelengths of the *HST/WFPC2*, *NICMOS* and *IRCS* filter systems. The optical constants are taken from BE amorphous carbon of Zubko et al. (1996). Monochromatic extinction in the visible, a huge extinction drop between 2 to 3 μm , and less extinction at longer than L' are best reproduced by 0.2 μm size grains.

Fig. 10.— A blow up of the central $4'' \times 4''$ region of AFGL 2688 at L' . The orientation of the dark lane is outlined by dashed lines to contrast with the axis of optical bipolar nebula. The dotted lines trace the local minimum of the image. The locations of peak A and the central star (source B) are marked with circles. The position of the central star is from the polarization mapping of Weintraub et al. (2000) and multiple CO outflow observations of Cox et al. (2000). The formal uncertainty in the position of source B by Weintraub et al. (2000) is $\lesssim 0''.03$, and the uncertainty in the radio observation by Cox et al. (2000) is $\lesssim 1''$.

Fig. 11.— The near-infrared SED of peak A and the adjacent regions. A series of aperture photometry was made at the both sides of peak A from $0''.5$ southeast to $2''.3$ to northeast with 10 pixels ($0''.583$) aperture and separation.

Fig. 12.— The 3 μm spectra of AFGL 2688 normalized to the power-law continuum defined in Fig. 5. The overlay is a template spectrum to show how similar all of the spectra are.

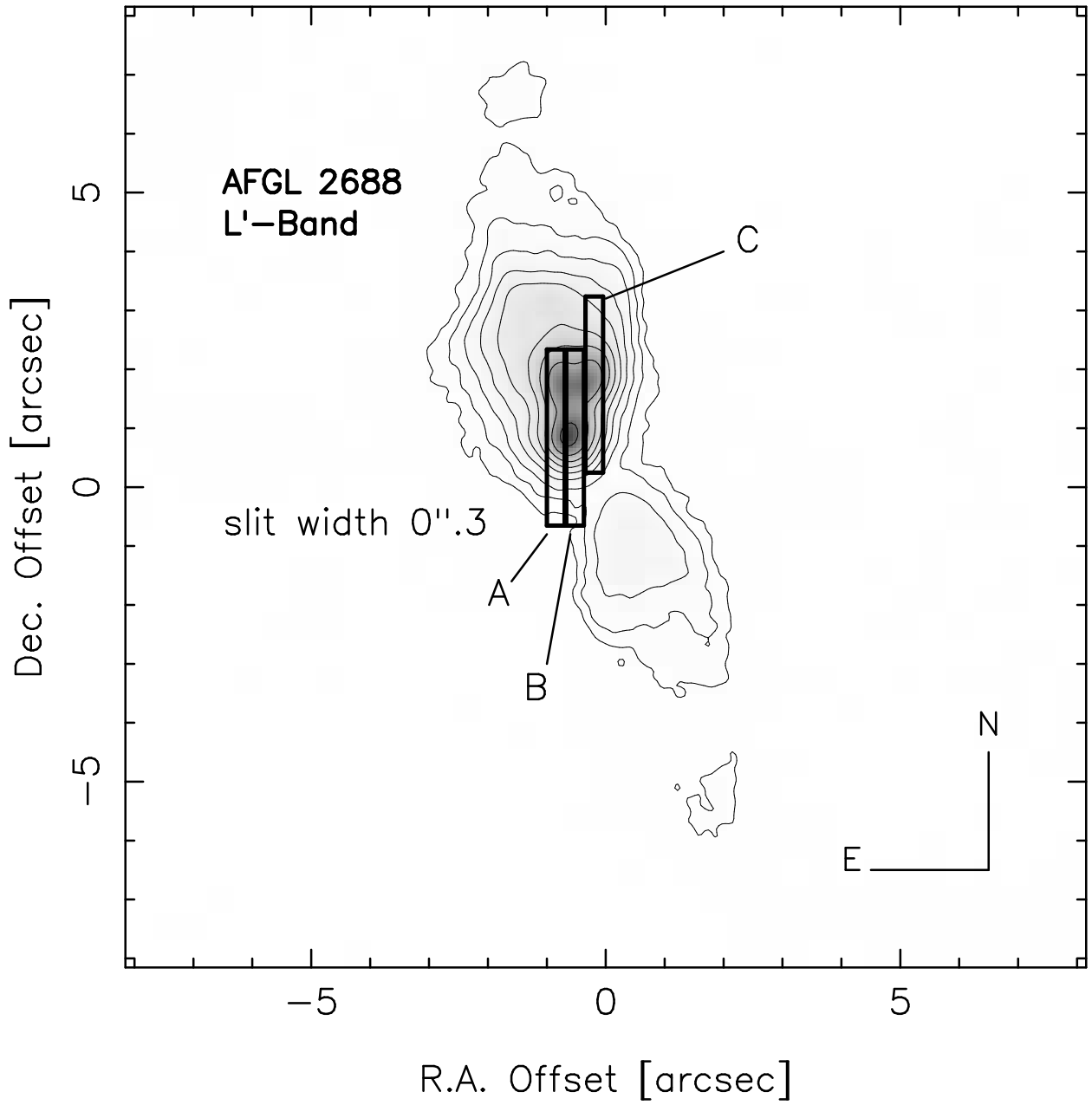


Fig. 4.—

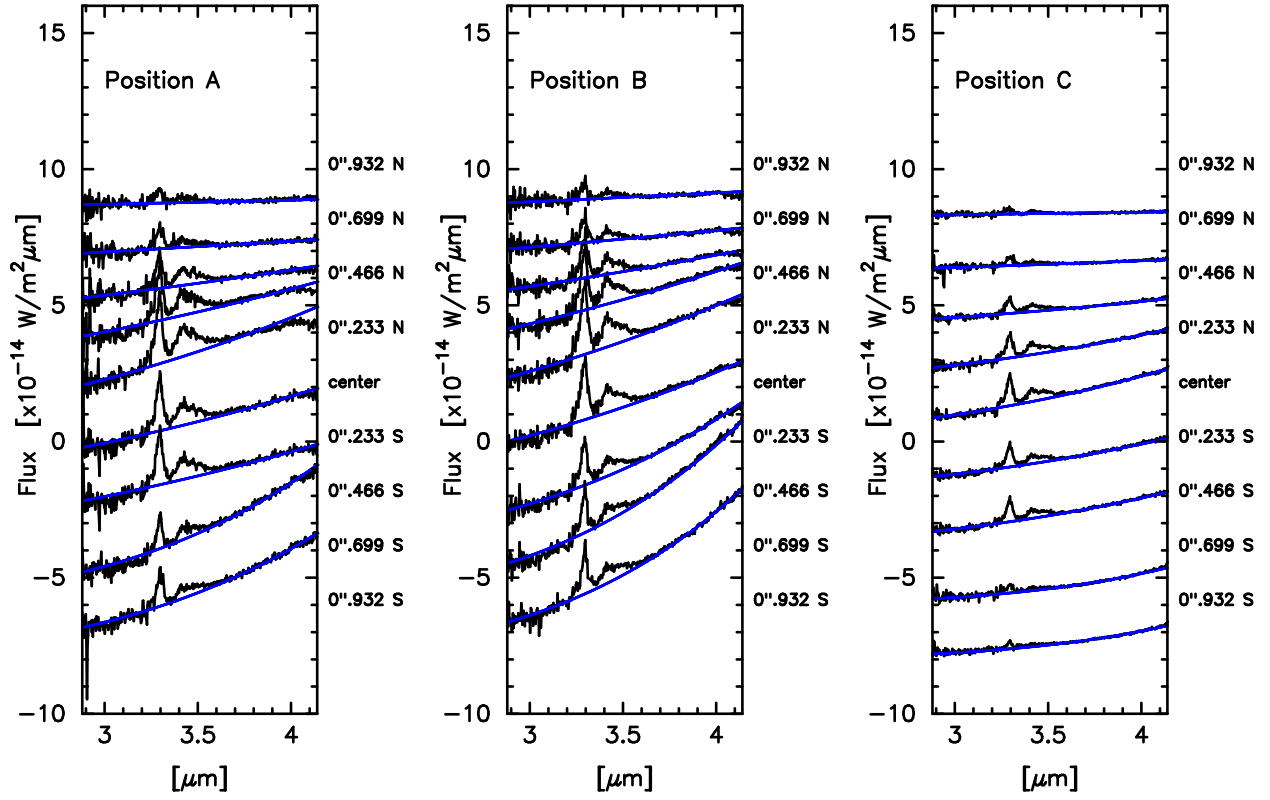


Fig. 5.—

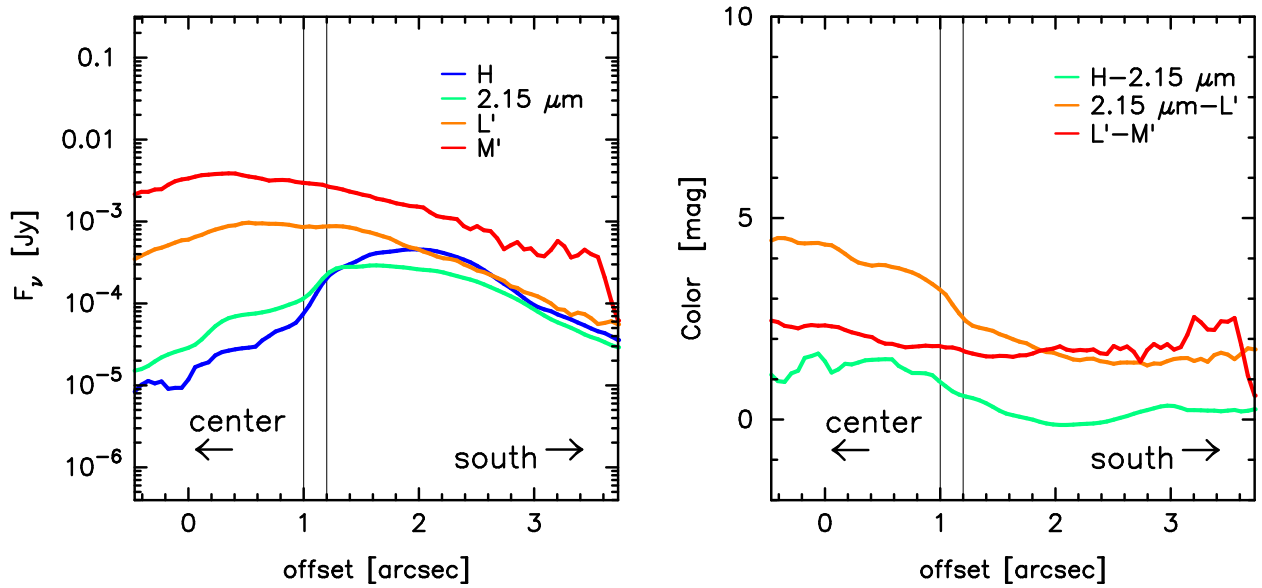


Fig. 7.—

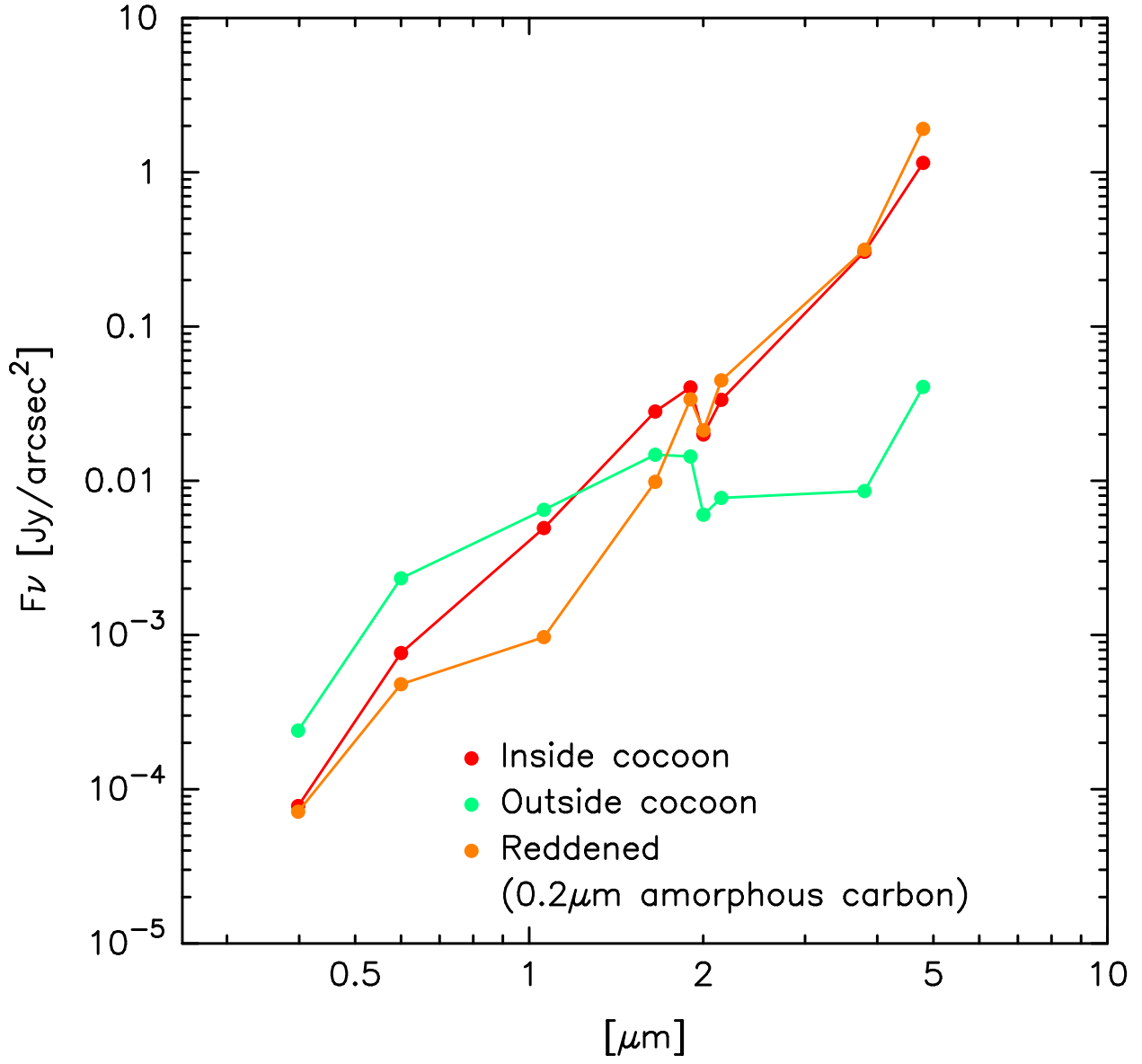


Fig. 8.—

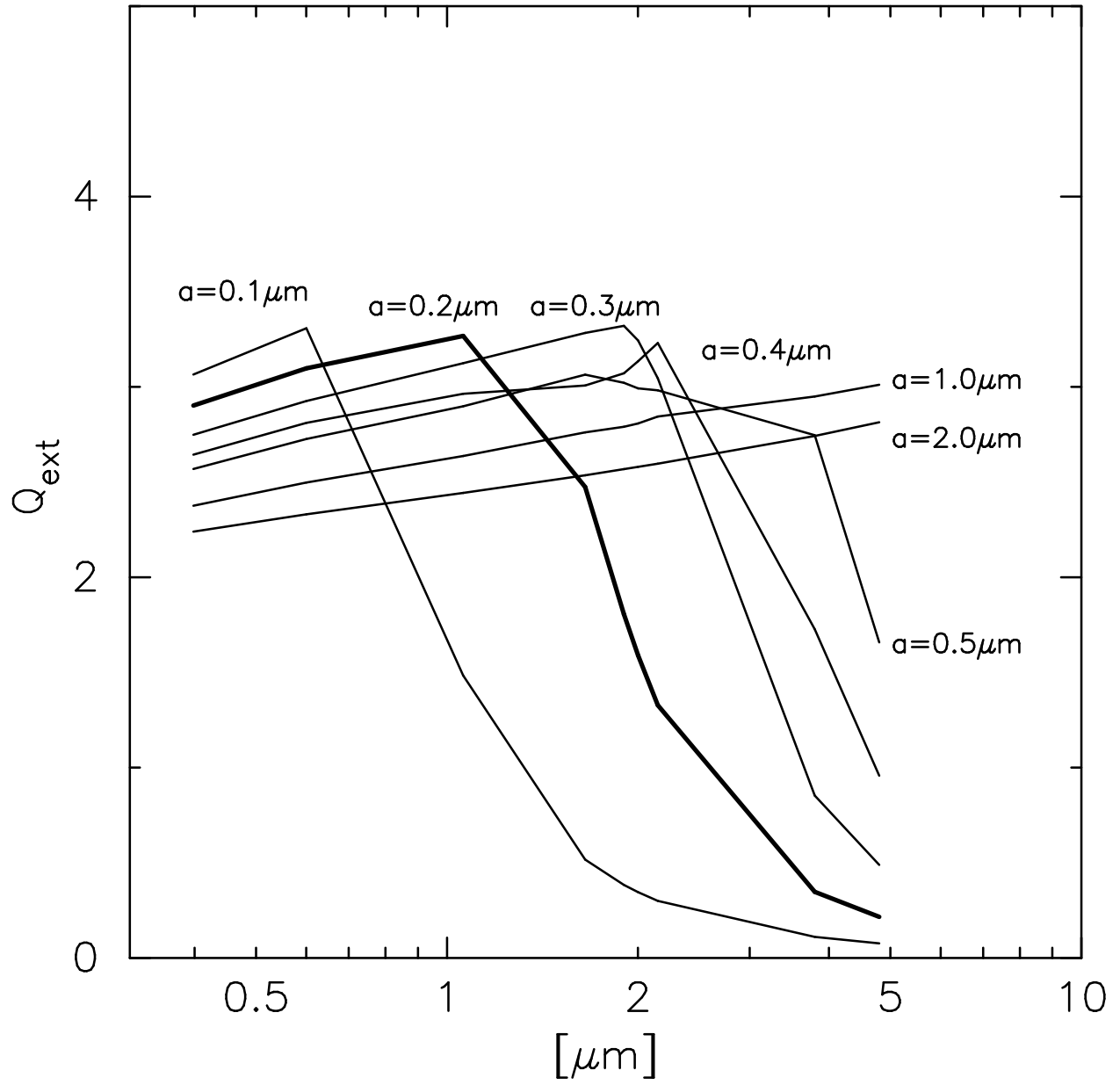


Fig. 9.—

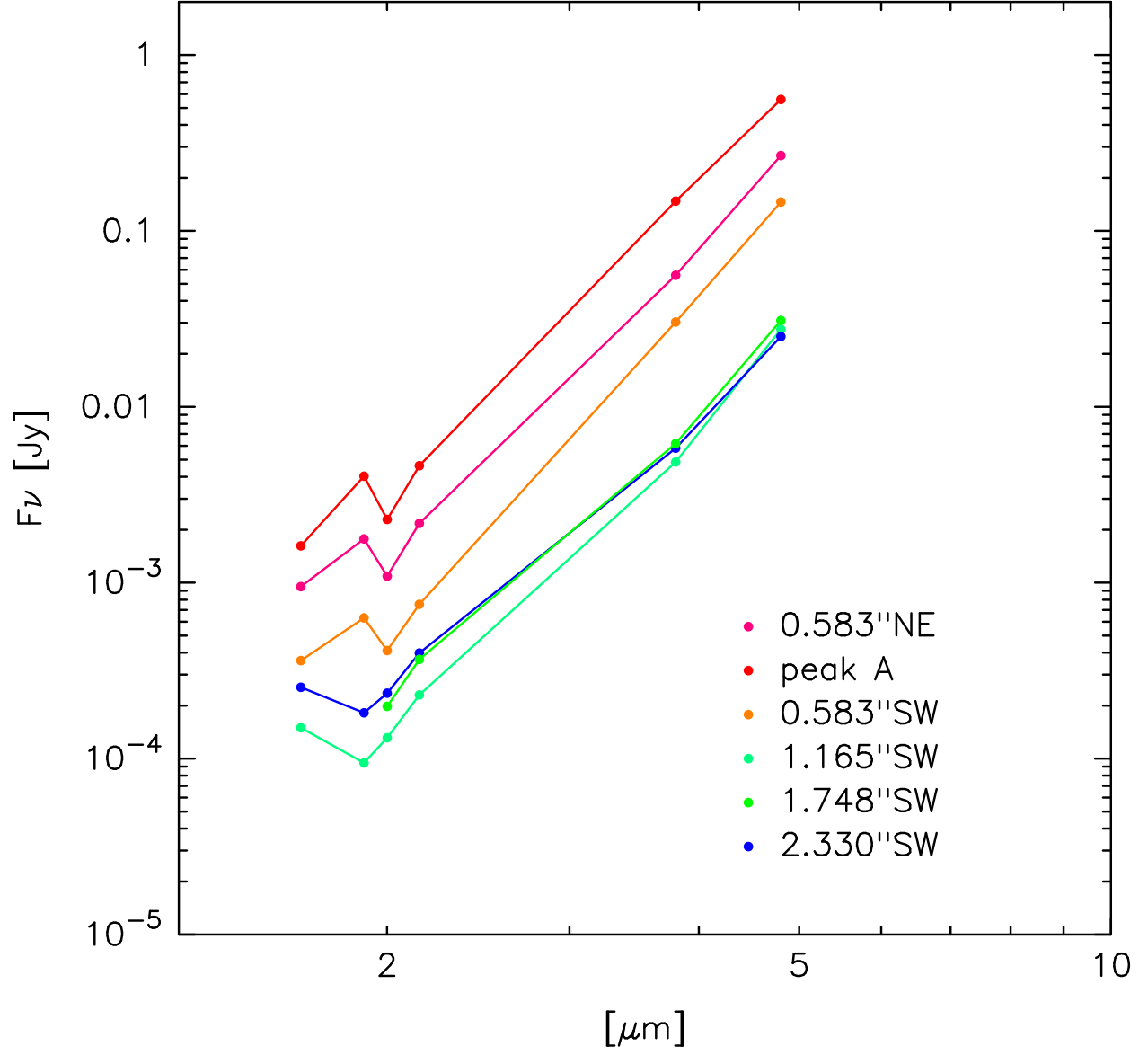


Fig. 11.—

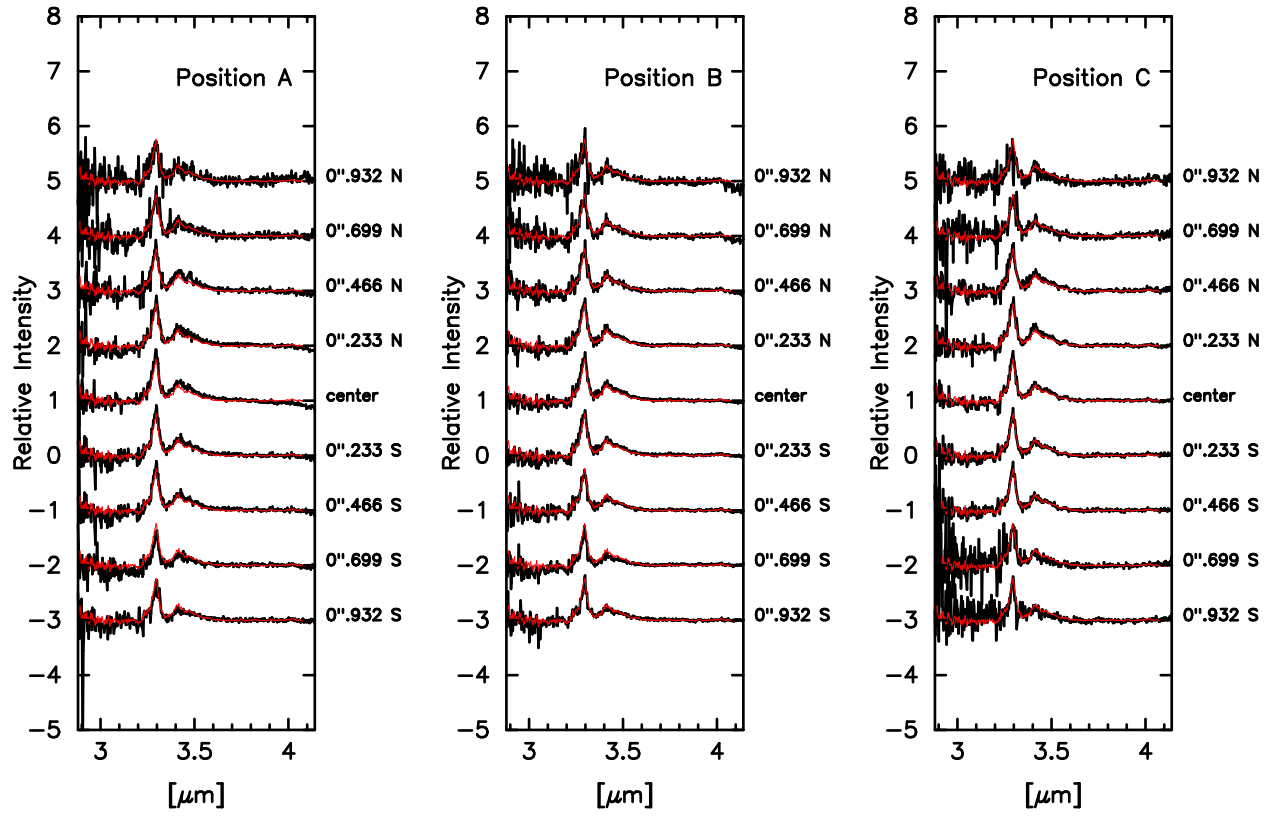


Fig. 12.—

This figure "f1a.jpg" is available in "jpg" format from:

<http://arxiv.org/ps/astro-ph/0202121v1>

This figure "f1b.jpg" is available in "jpg" format from:

<http://arxiv.org/ps/astro-ph/0202121v1>

This figure "f2a.jpg" is available in "jpg" format from:

<http://arxiv.org/ps/astro-ph/0202121v1>

This figure "f2b.jpg" is available in "jpg" format from:

<http://arxiv.org/ps/astro-ph/0202121v1>

This figure "f3a.jpg" is available in "jpg" format from:

<http://arxiv.org/ps/astro-ph/0202121v1>

This figure "f3b.jpg" is available in "jpg" format from:

<http://arxiv.org/ps/astro-ph/0202121v1>

This figure "f6.jpg" is available in "jpg" format from:

<http://arxiv.org/ps/astro-ph/0202121v1>

This figure "f10.jpg" is available in "jpg" format from:

<http://arxiv.org/ps/astro-ph/0202121v1>